

Direct3 γ : a Pipeline for Direct Three-gamma PET Image Reconstruction

Youness Mellak, Alexandre Bousse, Thibaut Merlin, Debora Giovagnoli, Dimitris Visvikis

Abstract—This paper presents a novel image reconstruction pipeline for three-gamma ($3\text{-}\gamma$) positron emission tomography (PET) aimed at improving spatial resolution and reducing noise in nuclear medicine. The proposed Direct3 γ pipeline addresses the inherent challenges in $3\text{-}\gamma$ PET systems, such as detector imperfections and uncertainty in photon interaction points. A key feature of the pipeline is its ability to determine the order of the detected photons to construct Compton cones, which intersect with the line of response (LOR) to provide an estimation of the emission point. The pipeline processes $3\text{-}\gamma$ PET raw data, reconstructs histo-images by propagating energy and spatial uncertainties along the LOR, and applies a 3-D convolutional neural network (CNN) to refine these intermediate images into high-quality reconstructions. To further enhance image quality, the pipeline leverages both supervised learning and adversarial losses, with the latter preserving fine structural details. Experimental results demonstrate that Direct3 γ consistently outperforms conventional 200-ps time-of-flight (TOF) PET in terms of SSIM and PSNR. This pipeline provides a robust framework for $3\text{-}\gamma$ -PET imaging, enabling more accurate localization of emission points and setting the stage for improved diagnostic capabilities in clinical and research settings.

Index Terms—Three-gamma PET, Direct reconstruction, Histo-images, Gamma-ray tracking, GNN.

I. INTRODUCTION

SINCE the early 2000s the idea of $3\text{-}\gamma$ imaging in PET has been considered. It is based on the utilization of radioisotopes that emit a positron and almost simultaneously an additional gamma photon. Such popular non-pure positron emitters include ^{124}I (half-life=4.176d, emission of 602.7 keV photon) and ^{44}Sc (half-life=4.176d, emission of 1,157 keV photon) which have been associated with multiple clinical applications in oncology and more specifically in the field of theranostics [1], [2].

The idea of $3\text{-}\gamma$ PET imaging is based on the general concept of a Compton camera, where the detection of a Compton scatter and associated kinematics is used for the reconstruction of the source position. The positron annihilation with an electron in the tissue produces the two 511-keV photons defining the coincidence LOR is used in conventional

PET imaging. Through the emission of the additional (third) gamma, Compton interactions in the detector can be used to define a Compton cone using Compton kinematics. The cone is drawn based on the first two interactions of the third gamma in the detector. More specifically, the aperture angle of the cone is given as the Compton angle of the first interaction while the axis of the cone is the line connecting the two interactions. The intersection between the cone and the LOR can be subsequently used to provide additional information about the source position (cf., Figure 1). In principle the advantages of such an approach relative to standard PET imaging include an improvement in overall sensitivity as well as better image resolution [3].

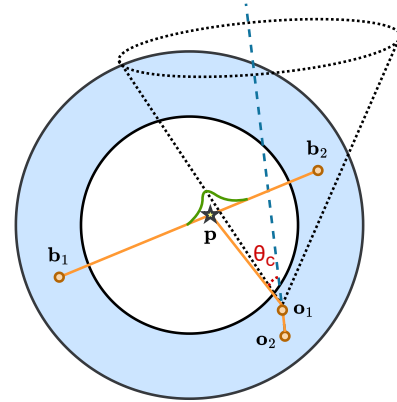


Fig. 1: Estimating the point of emission using Compton kinematics. b_1 and b_2 respectively the first and second photon detected positions resulting from the annihilation (back-to-back photons) while o_1 and o_2 are respectively the first and second interaction positions of the prompt gamma in the detector. The yellow star indicates the real emission point.

Two different detector systems have been developed over the past two decades for the implementation of such $3\text{-}\gamma$ PET imaging systems. The first one concerns the development of a liquid xenon (LXe) Compton camera (e.g., the Xenon Medical Imaging System (XEMIS) project [4]) where the LXe acts as the scatterer and detection medium for the third photon but also for the two back-to-back 511-keV photons [5]. The second one involves the utilization of a dual-detector structure combining PET and Compton imaging, with the second detector acting as the scatterer [3], [6]. However, these systems do not determine the order of the interactions in the detector.

This work did not involve human subjects or animals in its research.

All authors declare that they have no known conflicts of interest in terms of competing financial interests or personal relationships that could have an influence or are relevant to the work reported in this paper.

This work has received a French government support granted to the Comin-labs excellence laboratory and managed by the French National Research Agency (ANR) in the “Investing for the Future” program under reference ANR-10-LABX-07-01.

All authors are affiliated to the LaTIM, Inserm, UMR 1101, *Université de Bretagne Occidentale*, Brest, France.

Corresponding author: A. Bousse, bousse@univ-brest.fr

Recent advancements in 3- γ imaging reconstruction techniques have aimed to enhance image quality while utilizing low statistics. Giovagnoli *et al.* [7] introduced a method that uses the intersection point of the Compton cone and two coincidence photons of the LOR as the center for a probability density function (PDF), similar to TOF PET. Yoshida *et al.* [8] proposed a scanner design with separate scatterer and absorber modules, incorporating scatter angle calculations using the Klein-Nishina (KN) formula and modeling blurring with asymmetric Gaussian functions. Both approaches rely on identifying the LOR-Compton cone intersection point, but face challenges in determining the order of prompt gamma interactions. Yoshida’s scatter-absorber design addresses this through hardware modifications and energy windowing, albeit at the cost of reduced sensitivity. In contrast, the XEMIS-like scanner uses a single dense ring of LXe, where prompt gammas interact multiple times until absorption. This design, while promising, lacks a built-in mechanism for determining interaction order and is susceptible to errors from spatial resolution limitations and Doppler effects, especially given the proximity of interaction points.

Our proposed method, Direct3 γ , presents a structured pipeline for reconstructing 3-D 3- γ PET images on an event-by-event basis. This approach consists of three main stages, as illustrated in Figure 2:

- (i) Event detection and Compton cone construction: We start by detecting raw 3- γ events from the scanner data. Next, we use a graph neural network (GNN)-based architecture, called modified interaction network (MIN), to sequence the interactions of photons. Finally, we construct the Compton cone based on first and second interactions.
- (ii) LOR processing and histo-image generation: This stage incorporates blurring effects on the LOR using the detector response error propagator (DREP) method, accounts for detection system uncertainties, applies attenuation correction, and generates a histo-image as a preliminary representation of the activity distribution.
- (iii) Image reconstruction and enhancement: The final stage employs an encoder-Decoder CNN for image processing, performing both deblurring and denoising to enhance image quality.

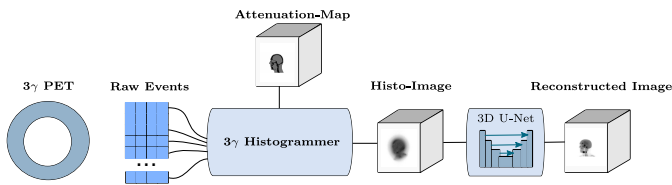


Fig. 2: Direct3 γ pipeline, from event detection, building histo-image using the histogrammer and the backbone to reconstruct the final image.

Various approaches have been proposed to address the challenges in stage (i). Oberlack *et al.* [9] presented an algorithm to reconstruct Compton scattering sequences by minimizing a $d\phi$ -criterion among $N!$ possible sequences. Pratz *et al.* [10] introduced a Bayesian approach utilizing additional information about photon interactions and detector

characteristics. While effective, these methods are computationally expensive. Zoglauer *et al.* [11] developed a neural network (NN) to improve efficiency, but it remains limited for complex scenarios ($N > 4$). To overcome these limitations, we propose two novel approaches. Firstly, a GNN inspired by Andersson [12], using a modified interaction network (IN) to classify edges and determine the prompt gamma’s path in the detector. Secondly, we introduce an order-less approach that estimates intersection points using all potential sequences, addressing accuracy issues in complex scenarios.

For stage (ii), we build upon previous work in incorporating detector uncertainties. Giovagnoli *et al.* [7] propagated spatial and energy uncertainties to angle uncertainties, modeling them as symmetric Gaussians on the LOR. Yoshida *et al.* [8] proposed the use of a non-symmetric Gaussian and noted that the position estimations are highly accurate when this angle is close to 90° . However, as the angle approaches 0° , the accuracy diminishes significantly, resulting in increased background noise when such positions are back-projected with the same intensity. They introduced a detector response function (DRF) model specifically designed to incorporate the blurring effects along the LOR that arise from energy resolution discrepancies. Our DREP module extends these concepts, propagating energy resolution (modeled as a Gaussian distribution with 9% full width at half maximum (FWHM) for 511-keV photons in XEMIS) and spatial uncertainties (uniform distribution within 3.125 mm^3 voxels) to estimate Compton angle uncertainty. We then construct the histo-image by back-projecting the estimated asymmetric Gaussians.

For stage (iii), we employ a 3-D model capable of doing image to image translation mapping histo-images to real emission sites in approximately real time.

This paper is structured as follows: Section II details the complete pipeline from raw data to reconstructed images. Section III presents the results of reconstructed images using the proposed pipeline. Section IV discusses limitations, potential improvements and alternative approaches. Finally, Section V concludes this paper.

II. METHOD

The objective is to reconstruct an 3-D activity image $x \in \mathbb{R}^P$ where P is the number of voxels in the field of view (FOV), from a collection of K 3- γ detection events.

A. Photon Interaction Sequence Determination

In this section we describe our approach to determine the photon interaction sequence determination, which is then used to draw the Compton cone. While the standard approach consists in considering events with two interactions only (which represents $\approx 30\%$ of the events) and assuming that the interaction with the largest energy deposit is the first (which is not guaranteed), our approach is designed to process events with more than two interactions.

A prompt gamma detection event is represented by a collection of N events (in unknown order), $\mathbf{o}_1 = (\mathbf{r}_1, E_1), \dots, \mathbf{o}_N = (\mathbf{r}_N, E_N)$ where for all $k = 1, \dots, N$, $\mathbf{r}_k = (x_k, y_k, z_k) \in \mathbb{R}^3$ is the 3-D location of the k th

interaction and E_k , $k \geq 1$ is the deposited energy at the k th interaction. In addition to the prompt gamma, two back-to-back 511-keV gamma rays are emitted and are detected at b_1 and b_2 (see Figure 1).

Considering that a prompt gamma interacts N times in the detector, i.e., $N-1$ Compton scatters interactions followed by a final photo-absorption, there are $N!$ possible paths. We first describe the $d\phi$ -criterion approach (Section II-A1) and a conventional NN approach from the literature (Section II-A2). We then, introduce our proposed MIN (Section II-A3).

1) *The $d\phi$ -criterion*: In Compton kinematics, the relationship between the k th scattering angle θ_k^{kin} , $k = 1, \dots, N-2$ (N points define $N-2$ angles) and the deposited energy is given by the Compton scattering equation, i.e.,

$$\cos \theta_k^{\text{kin}} = 1 - \frac{m_e c^2 E_{k+1}}{E_k (E_k - E_{k+1})}$$

where m_e is the mass of an electron and c is the speed of light. The $d\phi$ -criterion [9] evaluates the fit between the geometric angles θ_k^{geom} (determined by a given sequence of interactions) and θ_k^{kin} , $k = 1, \dots, N-2$, as

$$d\phi = \sum_{k=1}^{N-2} (\cos \theta_k^{\text{kin}} - \cos \theta_k^{\text{geom}})^2. \quad (1)$$

The photon interaction sequence is determined by minimizing (1), which is achieved by computing all possible sequences. Note that the solution is not necessarily unique.

2) *Fully-Connected Neural Network*: Multi-layer feed-forward NNs are universal function approximators. Zoglauer *et al.* [11] proposed an architecture that takes as input the normalized deposited energy and positions of interactions with other statistics obtained via simulation such as the Compton scatter angle, the measured total energy, the $d\phi$ -criterion, the distance between the interactions, as well as the absorption and scatter probabilities and the number of interactions. The fully-connected neural network (FCNN) contains one hidden layer whose task is to classify the right sequence, such that the output layer contains $N!$ neurons, each of which referring to a possible path with a given probability—the path with highest probability is then chosen. Zoglauer *et al.* showed that this type of network is suitable for events with $N = 3$ or 4 interactions but may diverge with for $N > 4$ due to the complexity.

We implemented a modified version of the architecture proposed by Zoglauer *et al.* (Figure 3) with deeper layers and which is trained on deposited energy and position coordinates only, without providing additional information about other statistics. This simplified architecture is easier to train and will be used for comparison (Section III-B).

3) *Modified Interaction Network for Sequence Reconstruction (Proposed Method)*: In their original paper, Battaglia *et al.* [13] proposed an architecture, namely interaction network (IN), which takes a directed graph as input and outputs values associated to the nodes, edges or the entire graph (e.g., graph classification). The method proved to be a powerful general framework for modeling objects and relations between them.

Andersson [12] proposed a GNN framework for gamma-ray track reconstruction in germanium detector arrays. The

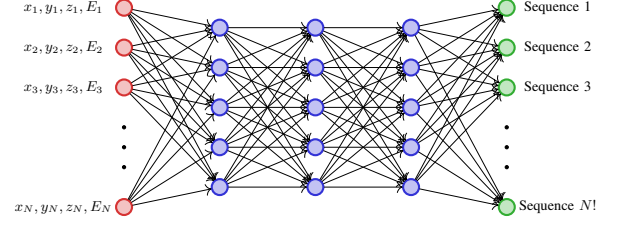


Fig. 3: FCNN architectures for photon path estimation: where x_i, y_i, z_i are the normalized coordinates of each hit, E_i the deposited energy,

position of the interaction source is known, and the network is tasked with determining the positions and energies of gamma interactions within the detector. The network must also disentangle and build separate tracks for different gamma photons that are emitted simultaneously, ensuring accurate reconstruction even in complex scenarios with multiple interactions. In our case the initial emission is unknown: only N interactions of a single photon that arrives on a region of a detector is known. We propose a simple GNN architecture using the framework proposed in [13].

We consider a collection of N nodes $\mathbf{o}_1, \dots, \mathbf{o}_N$, with N_f features, i.e., for all $k = 1, \dots, N$, $\mathbf{o}_k \in \mathbb{R}^{N_f}$, and $N_e = N(N-1)$ possible edges (see Figure 11(a) for the $N = 3$ case). The nodes are concatenated in a matrix $\mathbf{O} = [\mathbf{o}_1^\top, \dots, \mathbf{o}_N^\top]^\top \in \mathbb{R}^{N \times N_f}$ where ‘ \top ’ denotes the matrix transposition. In our case, $\mathbf{o}_k = (r_k, E_k)$ (the 3-D coordinates of the interaction and the deposited energy) and the number of features per node is $N_f = 4$. We propose a method based on INs to determine photon interaction sequences from \mathbf{O} . This approach treats the problem as an edge classification task on a graph-structured representation of the interactions. Note that for the purpose of Compton cone determination, only the two first interactions need to be determined.

The overall procedure, summarized in Figure 4 and fully described in Appendix A, defines a mapping $\mathbf{F}_\theta: \mathbb{R}^{N \times N_f} \rightarrow [0, 1]^{N_e}$ maps a sequence of interactions $(r_1, E_1), \dots, (r_N, E_N)$ to a N_e -dimensional fuzzy vector containing scores for each edge. Edges with a score lower than 0.5 are then removed, which returns the final graph (Figure 11(b) shows a possible output). This representation allows the model to learn complex patterns of energy deposits and scattering angles without explicitly encoding physics rules [12]. GNNs can process variable numbers of interaction points per event. This approach also scales well to large numbers of interaction points better than the FCNN.

Note that \mathbf{F}_θ does not discard non-admissible graphs, that is to say, containing V-structures (two edges departing from one node or two edges pointing to one node) and cycles. However, as we will see in Section III-B, a well-trained network is unlikely to return such graphs. In addition, the architecture of \mathbf{F}_θ does not guarantee that two permutation-equivariant collections of nodes \mathbf{O} and \mathbf{O}' are mapped to the same graph. We will also show in Section III-B that the same graphs (after binarisation) are obtained in most cases.

The model is trained from a collection of interaction/graph

pairs (\mathbf{O}, \mathbf{y}) , $\mathbf{y} \in \{0, 1\}^{N_e}$ being a binary vector corresponding to the true sequence of interaction such that $[\mathbf{y}]_\ell = 1$ if the edge \mathbf{y}_ℓ is present and $[\mathbf{y}]_\ell = 0$ otherwise (for example in Figure 11(b) the graph corresponds to $\mathbf{y} = [0, 0, 1, 0, 0, 1]^\top$), obtained from Monte Carlo (MC) simulations, by minimizing the cross-entropy between the estimated (fuzzy) graph $\mathbf{F}_\theta(\mathbf{O})$ and \mathbf{y}

$$\min_{\theta} \mathbb{E}_{(\mathbf{O}, \mathbf{y})} [\mathcal{L}(\mathbf{F}_\theta(\mathbf{O}), \mathbf{y})],$$

$$\mathcal{L}(\mathbf{z}, \mathbf{y}) \triangleq - \sum_{l=1}^{N_e} y_l \log z_l + (1 - y_l) \log(1 - z_l) \forall \mathbf{y}, \mathbf{z} \in \mathbb{R}^{N_e}.$$

B. Histo-image Generation

1) *Emission Point Estimation*: Using the first two interactions of the prompt gamma \mathbf{o}_1 and \mathbf{o}_2 (which were determined using MIN, cf. Section II-A3), the initial energy $E_{\text{init}} = 1.157$ MeV and the deposited energy E_1 in the first interaction, the Compton cone can be determined. The cone's angle $\theta_c \in [-\pi/2, \pi/2]$ is calculated using the KN formula:

$$\cos(\theta_c) = 1 - \frac{m_e c^2 E_1}{E_{\text{init}}(E_{\text{init}} - E_1)} \quad (2)$$

The cone's vertex is positioned at the first interaction point of the photon, and its axis runs through to the second interaction point (Figure 1).

The emission point of a prompt gamma can be estimated as the intersection point $\mathbf{p} \in \mathbb{R}^3$ between the Compton cone and the LOR given by the two points \mathbf{b}_1 and \mathbf{b}_2 , i.e., by solving

$$\frac{(\mathbf{p} - \mathbf{r}_1) \cdot \mathbf{n}}{\|\mathbf{p} - \mathbf{r}_1\|_2} = \cos(\theta_c).$$

where \mathbf{n} is the directional (unitary) vector from \mathbf{o}_2 to \mathbf{o}_1 .

2) *Modeling Spatial Uncertainty*: However, the use of this method faces challenges due to detector imperfections. In the case of the XEMIS-2 detector, significant uncertainties exist in both energy and spatial measurements. The detector exhibits an energy resolution of 9% FWHM for 511-keV γ -rays, modeled as a Gaussian distribution around measured energy values. The intrinsic spatial resolution is determined by the detector size and assumed to follow a uniform distribution.

Translating the uncertainties associated with the detector's measurements to the cone angle θ_c results in uncertainty around the estimated point \mathbf{p} on the LOR. However, using a symmetric error model around the estimated point, as described in Giovagnoli *et al.* [7], is not the most effective method for projecting this error from the Compton cone to the LOR. The uncertainty along the LOR is influenced by several factors, including the crossing angle between the Compton cone and the LOR as well as the distance between the vertex of the cone and the LOR. Drawing inspiration from the findings in Yoshida *et al.* [8], we propose applying a non-symmetric Gaussian distribution around the estimated point.

Our model uses the σ_{mix}^+ and σ_{mix}^- standard deviations (STDs) calculated by DREP (cf. Appendix B, Equation (4)

and Equation (5)) to define a collection of ‘‘histo-functions’’ $h_{\mathbf{p}}$ for all of the K events. The mathematical formulation is:

$$h_{\mathbf{p}}(t) = \begin{cases} \frac{1}{\sqrt{2\pi(\sigma_{\text{mix}}^+ + \sigma_{\text{mix}}^-)}} \exp\left(-\frac{(t-t_0)^2}{2(\sigma_{\text{mix}}^-)^2}\right) & \text{for } t < t_0, \\ \frac{1}{\sqrt{2\pi(\sigma_{\text{mix}}^+ + \sigma_{\text{mix}}^-)}} \exp\left(-\frac{(t-t_0)^2}{2(\sigma_{\text{mix}}^+)^2}\right) & \text{for } t \geq t_0. \end{cases} \quad (3)$$

where t_0 is the position of \mathbf{p} along the LOR defined by \mathbf{b}_1 and \mathbf{b}_2

3) *Three-gamma Histogrammer*: We define a 3- γ histogrammer using a non-symmetric Gaussian PDF to model emission event distribution along the LOR. This approach extends the Most Likely Annihilation Position histogrammer proposed by Whiteley *et al.* [14] for TOF PET. The 3- γ histo-image is created by summing voxelized P -dimensional versions of the $h_{\mathbf{p}}(t)$ for each estimated location \mathbf{p} , P being the number of voxels, resulting in a P -dimensional radioactivity image.

4) *Attenuation Correction*: In 3- γ PET imaging with ^{44}Sc , we need to correct for attenuation of 511 keV and 1,157 keV gamma rays. The attenuation correction factors $a_{\mathbf{p}}$ for each \mathbf{p} is given by

$$a_{\mathbf{p}} = e^{\int_{b_1}^{b_2} \mu_{511}(\mathbf{r}) d\mathbf{r}} \cdot e^{\int_{\mathbf{p}}^{\mathbf{o}_1} \mu_{1157}(\mathbf{r}) d\mathbf{r}}$$

where $\mu_{511}(\mathbf{r})$ and $\mu_{1157}(\mathbf{r})$ are the attenuation coefficients at position $\mathbf{r} \in \mathbb{R}^3$ for 511 keV and 1,157 keV gamma rays, respectively. The attenuation-corrected histo-function is

$$h_{\mathbf{p}}^{\text{att}}(x) = a_{\mathbf{p}} \cdot h_{\mathbf{p}}(t)$$

C. From the Histo-image to the Final Image

Equation (3) can result in two possible intersection points between the Compton cone and the LOR within the FOV. Both of these solutions are utilized in the creation of histo-images, which leads to noise caused by false positives in the image. Another possible source of noise is inaccuracies in the algorithm that is responsible for determining the sequence of detected gamma rays. Furthermore, we need to correct for the uncertainty along the LOR in the histo-images.

To address the issue of blurring and noise in histo-images, we propose the use of a simple U-Net architecture as the backbone for our image-to-image translation tasks (the full pipeline is illustrated in Figure 2). In this work, we implemented a generative model, which combines the U-Net architecture with a patch discriminator and a least squares GAN (LS-GAN) loss function, following the approach of Isola *et al.* [15] and Cirillo *et al.* [16]. In this generative framework, the U-Net $G_{\psi}: \mathbb{R}^P \rightarrow \mathbb{R}^P$ with parameter ψ maps histo-images $\mathbf{x} \in \mathbb{R}^P$ to the true emission images $\mathbf{x}^* \in \mathbb{R}^P$. The model learns to refine the image by reducing noise and blur, while the patch-based discriminator with adversarial training ensures that the output images hold high-frequency details.

III. EXPERIMENTS AND RESULTS

A. Detector Setup and Datasets

1) *Detector*: Data acquisition was carried out using simulations implemented through Geant4 Application for Tomography Emission (GATE) [17], focusing on two types of scanners:

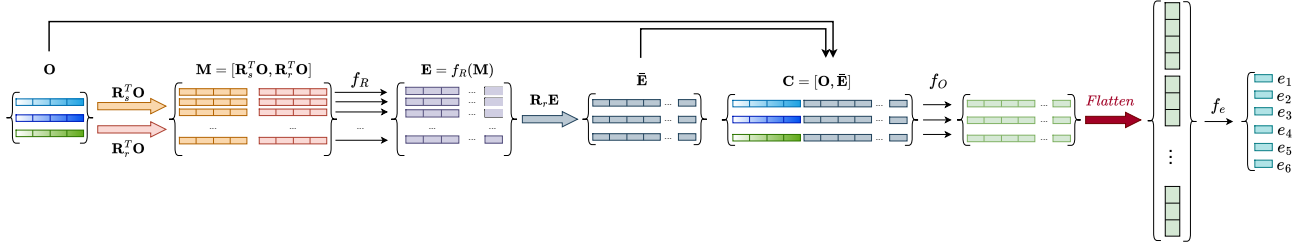


Fig. 4: MIN—Proposed architecture for F_θ used to classify edges or relations between photons interactions in the detector (see Appendix A).

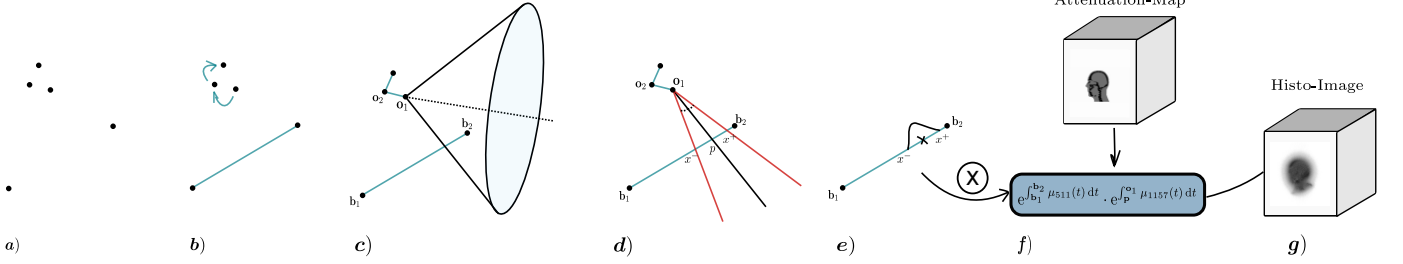


Fig. 5: Workflow of the Direct3 γ histogrammer: (a) detection of hits by the 3- γ PET scanner; (b) construction of LOR and determination of prompt gamma interaction order; (c) estimation of intersection between Compton cone and LOR; (d) calculation of uncertainties on the LOR; (e) projection of estimated Gaussian distribution onto image space; and (f) application of attenuation correction.

(i) a human-sized scanner with dimensions comparable to the Siemens mMR system and (ii) a small-animal pre-clinical scanner XEMIS2 [18]–[20]. The human-sized scanner featured an inner diameter of 60 cm and an outer diameter of 90 cm, with its detection system modified to employ LXe as in the XEMIS series. For both scanners, the pixel size was set at $3.125 \times 3.125 \text{ mm}^2$, while the longitudinal spatial resolution was maintained below $100 \mu\text{m}$. The energy resolution for both systems was approximately 9% FWHM at 511 keV, adhering to the specifications of the XEMIS2 scanner. For simulations incorporating conventional TOF, a smaller scanner with the same dimensions as the XEMIS2 but equipped with LSO crystals of size of $1 \times 1 \times 10 \text{ mm}^3$ was employed. In the case of the larger scanner, an mMR system was utilized for comparative purposes.

2) Training and Evaluation Datasets:

a) Experiment 1—Photon Interaction Sequence Determination: To train MIN and the FCNN, we conducted a simulation using a uniform cylinder in the FOV. This simulation produced up to 20 million 3- γ events. We only included events where all gamma rays fully interacted with the detector, meaning the sum of deposited energies across all interactions equaled 1.157 MeV. We created different MINs and FCNNs based on the number of interactions in each event. For testing, we used a separate dataset of 2 million events, also generated from a uniform cylinder in the FOV.

To train the MIN and FCNN models, a simulation was conducted using a uniform cylindrical object within the FOV. This simulation generated up to 20 million 3- γ events, with only those events included where all gamma rays fully interacted with the detector, ensuring that the total deposited energy across all interactions equaled 1.157 MeV. Separate models of

MIN and FCNN were created, each tailored to the number of interactions per event. For testing, a distinct dataset of 2 million events, also derived from a uniform cylinder within the FOV, was employed.

b) Experiment 2—Image Reconstruction: A set of 200 Extended Cardiac-Torso (XCAT) phantoms [21] was used to simulate ^{44}Sc activity along-side their 511-keV and 1,157 keV attenuation maps. These phantoms were designed with dimensions of $200 \times 200 \times 200$ voxels, with a voxel size of $3 \times 3 \times 3 \text{ mm}^3$ for the large scanner and $0.8 \times 0.8 \times 0.8 \text{ mm}^3$ for the small scanner (to produce mouse-sized XCAT phantoms), allowing for the representation of a wide range of anatomical sizes, shapes, and regions. To simulate diverse clinical scenarios, spherical lesions of various sizes and shapes were randomly introduced into different regions of the phantoms. For each phantom, between 5 and 20 million 3- γ events (excluding randoms and scatter coincidences), and the corresponding histo-images were produced using our histogrammer described in Section II-B3. The 3-D U-Net of Section II-C was then trained to map the histoimages to the real emission maps. To enhance model robustness and prevent overfitting, a data augmentation protocol was applied during the training process. This included random rigid transformations such as flipping, rotations, translations, and intensity rescaling within the range of 50% to 250%. The evaluation for the large scanner was conducted using five distinct XCAT volumes, each representing different body positions and varying activity levels. For the small scanner, we used a mouse phantom as well as four mouse-sized XCAT phantoms. Transverse views of these phantoms are presented in Figure 6.

The Direct3 γ reconstruction method was compared with conventional maximum-likelihood expectation-maximization

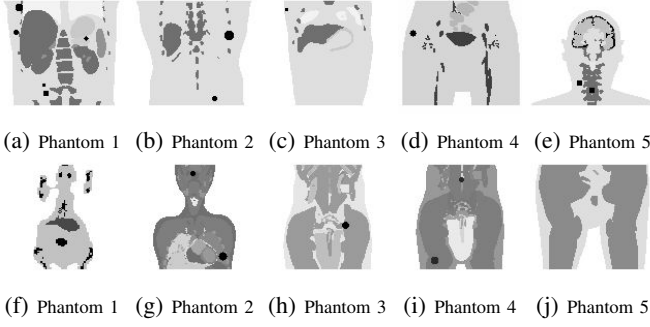


Fig. 6: Coronal views of (a)–(e) the human-sized phantoms ($3 \times 3 \times 3 \text{ mm}^3$ voxel size) and (f)–(j) the mouse-sized phantoms ($0.8 \times 0.8 \times 0.8 \text{ mm}^3$ voxel size) used in the test dataset.

algorithm (MLEM)-reconstructed images from 200-ps TOF PET data with and without deep image prior (DIP) post-processing [22], namely DIP-TOF. Similarly to training data, randoms and scatter coincidences were not included. We launched DIP with a 3-D U-Net for 600 epochs with a learning rate of $1e-3$ to balance structure preservation and prevent overfitting.

B. Experiment 1: Photon Interaction Sequence Determination

In this section we show the results on prediction of the order of interaction of the three methods described in Section II-A, i.e., $d\phi$ -criterion, FCNN and MIN (proposed approach), from the simulated data (Section III-A2a).

Table I presents the accuracy of the three algorithms in predicting photon interaction sequences. The table shows results for events with 3, 4, and 5 interactions. For events with only 2 interactions, no algorithm was applied; instead, we simply chose the position with the highest energy as the first interaction, resulting in approximately 81% accuracy. The table includes two additional columns: “All Events” and “First 2 only”. The “All Events” column represents the overall accuracy of reconstructing the entire interaction path for all events. The “First 2 only” column shows the accuracy of reconstructing just the first and second points of the sequence (needed for drawing the Compton cone). The accuracy is calculated as

$$\text{Accuracy} = \frac{\text{Number of well classified sequences}}{\text{Total number of events}}.$$

Approach	N=3	N=4	N=5	All Events	First 2 only
$d\phi$ -criterion	88	73.5	61	0.78	0.798
FCNN	91	82	59	0.80	0.82
MIN	93.5	92	77	0.864	0.877

TABLE I: Experiment 1—Comparison of the three different approaches ($d\phi$ -criterion, FCNN, MIN) for predicting the photon interaction sequence.

The results in Table I demonstrate that the MIN approach consistently outperforms the other two methods across all scenarios. It achieves the highest accuracy for events with 3, 4, and 5 interactions, as well as for overall events and when

considering only the first two interactions. As the number of interactions increases, the accuracy of all methods decreases, indicating that longer interaction sequences are more challenging to reconstruct. Interestingly, all methods show slightly higher accuracy when focusing on just the first two interactions, which is crucial for Compton cone reconstruction. It is important to note that MIN produced non-admissible sequences (V-structures, cycles) for 2% of the events, which were included into the accuracy calculations. Despite this limitation, MIN remains the most effective approach for predicting photon interaction sequences in this study.

C. Experiment 2: Image Reconstruction

The reconstructed images were assessed against the real emission map using SSIM and PSNR as quantitative evaluation metrics.

1) *Human-sized Scanner*: A comparison of reconstruction methods is presented in Figure 7. The results suggest that Direct3 γ consistently produces higher-quality images than both TOF and DIP-TOF. Direct3 γ provides clearer anatomical details and fewer errors compared to the ground truth (GT), particularly in the coronal and sagittal views, where contrast is better preserved and cold regions appear more distinct. While TOF offers sharper images, it introduces noise, and DIP-TOF, though effective in noise reduction, oversmooths important structures, leading to a loss of detail.

Figure 8 shows the scatter plot of the distribution of SSIM and PSNR values for all methods across the 5 multiple XCAT test phantoms. The Direct3 γ method consistently achieved superior SSIM values, ranging from 0.9399 to 0.9721, along with PSNR values between 26.15 and 35.40. In contrast, the classical TOF images exhibited lower SSIM values between 0.8708 and 0.9475, and PSNR values ranging from 25.74 to 34.37. A slight improvement in PSNR is observed with DIP-TOF images, with values ranging from 26.53 to 34.82 as DIP tends to reduce noise and smooth the reconstructed images. However, the SSIM values for DIP-TOF, ranging between 0.8612 and 0.9390, remain slightly lower than TOF images, likely due to the over-smoothing effect of DIP, which can reduce fine structural details. While DIP improved the noise characteristics (as reflected in higher PSNR), its impact on structural preservation was more modest, leading to only marginal improvements in SSIM compared to classical TOF.

2) *Mouse-sized Scanner*: A comparison between all reconstruction methods are presented in Figure 9. It shows that the Direct3 γ reconstruction offers a smoother image with fewer errors, though some finer details are missing compared to the GT. The TOF image suffers from significant noise, while the DIP-TOF image, though effective at noise reduction, oversmooths the image. In the error maps, the Direct3 γ method exhibits fewer and less intense errors compared to TOF and DIP-TOF, indicating a better balance between reducing error and maintaining image clarity.

Figure 10 shows a scatter plot for quantitative metrics for the 5 mouse-sized XCAT test phantoms. The results show Direct3 γ yielding higher SSIM values, ranging from 0.9302 to 0.9354, and PSNR values between 25.31 and 26.77. In

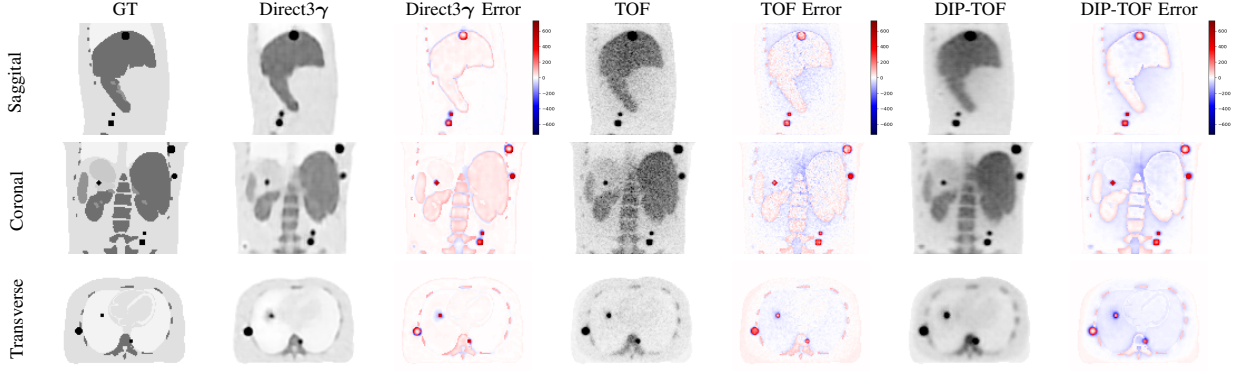


Fig. 7: Comparison of Direct3 γ , TOF and DIP-TOF for the large scanner.

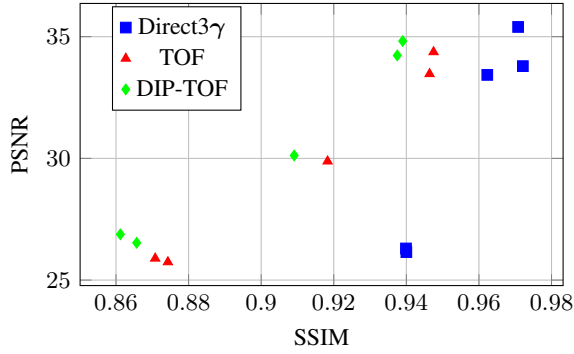


Fig. 8: Scatter plot illustrating the SSIM and PSNR values for Direct3 γ , MLEM 200-ps TOF and DIP-TOF, evaluated across the five human-sized phantoms (Figures 6(a)–(e)) used in this study for the large scanner.

comparison, the TOF images produced SSIM values ranging from 0.8881 to 0.8913, and PSNR values between 22.36 and 23.03. DIP-TOF displayed a slight improvement in terms of PSNR, with values ranging from 22.90 to 23.50. However, the DIP-TOF SSIM values ranging from 0.8825 to 0.8895, remained slightly lower than TOF due to over-smoothing effects.

IV. DISCUSSION

This study introduces a comprehensive approach to 3- γ PET imaging using ^{44}Sc , addressing key challenges in photon interaction sequence determination and emission point estimation. Our proposed MIN demonstrated superior accuracy in determining photon interaction sequences compared to both physical ($d\phi$ -criterion) and classical FCNN methods, particularly when complexity increase and number of interactions of the prompt gamma is more than 4. This improvement in sequence determination is crucial for Compton cone parameters determination thus accurate image reconstruction in 3- γ PET.

We introduced a novel DREP module and implemented a non-symmetric Gaussian function in our 3- γ histogrammer, both of which have demonstrated significant potential in improving the accuracy of emission event distribution modeling. The DREP module specifically addresses two key types of measurement uncertainties: energy resolution errors

and spatial position uncertainties. These uncertainties, inherent in PET detectors, can significantly impact the accuracy of Compton cone reconstruction and, consequently, the precision of emission point estimation. Our 3- γ histogrammer utilizes this non-symmetric Gaussian approach to more realistically represent the probability distribution of emission points along the LOR. This method accounts for the asymmetric nature of error propagation from the Compton cone to the LOR, a factor often overlooked in conventional symmetric models.

Furthermore, we introduced a custom attenuation correction technique specifically designed for ^{44}Sc -based 3- γ events. Unlike the standard attenuation correction applied in conventional PET, which deals only with the back-to-back annihilation photons, our approach accounts for the attenuation effects of both 511 keV annihilation photons and the 1.157 MeV prompt gamma ray emitted during ^{44}Sc decay. This dual-energy correction is essential, especially when considering larger or denser regions of interest, where photon attenuation is more prominent. By applying this correction step to the histo-images data prior to a NN for image reconstruction, we provide the network with more accurate inputs. This ensures that the NN focuses on mapping the true activity distribution, rather than compensating for physical effects like attenuation.

To address issues of histo-images coming from incorrect Compton cone estimation, and the presence of multiple estimated points on the same LOR, as well as low contrast due to the blurring effects introduced by DREP on LORs, we proposed a 3-D U-Net trained to map histo-images to real emission maps. Initial training of the network with only ones supervised loss resulted in blurred reconstructions. Therefore, we enhanced the training by integrating an adversarial loss component, which improved the preservation of fine details in the reconstructed images.

In both human-sized and small animal scanners, the Direct3 γ method demonstrates consistently better performance compared to both the TOF images and DIP-TOF images, particularly in terms of structural similarity and image clarity. This improvement can be attributed to the enhanced capabilities of the 3- γ system, in conjunction with the proposed DREP, which allows for more precise generation of histo-images and improved localization of the emission source. Furthermore, the integration of NNs, potentially augmented through adversarial

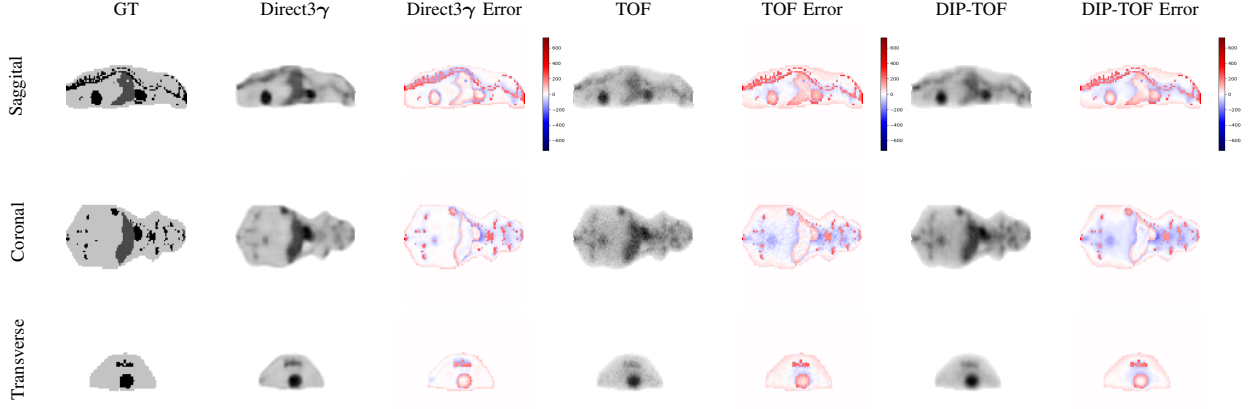


Fig. 9: Comparison of Direct3 γ , TOF and DIP-PET for small-animal scanner.

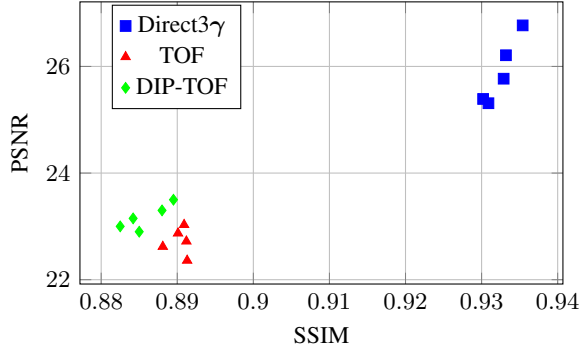


Fig. 10: Scatter plot illustrating the SSIM and PSNR values for Direct3 γ , MLEM 200-ps TOF and DIP-TOF, evaluated across the five mouse-sized phantoms (Figures 6(f)–(j)) used in this study for the small-animal scanner.

training, enhanced the reconstruction accuracy by refining noise reduction and structural fidelity. The DIP-TOF method offered a modest improvement in PSNR, due to its noise reduction capabilities, but the associated decline in SSIM can be linked to over-smoothing, which reduced the retention of structural details. In small animal scanners, the slight drop in SSIM and PSNR is likely caused by the reduction in voxel size used for reconstruction (from $3 \times 3 \times 3$ mm in large scanners to $0.8 \times 0.8 \times 0.8$ mm). This smaller voxel size leads to blurriness and loss of detail, which is due to the positron range effect, where positrons travel a short distance before annihilation, making it harder to maintain fine image resolution in smaller-scale scans.

V. CONCLUSION

this study presents a novel approach for reconstructing ac3g-PET images using ^{44}Sc , addressing key challenges in photon interaction sequence determination and emission event modeling. The proposed methods, particularly the MIN approach for photon ordering and the use of a non-symmetric Gaussian function in the histogrammer, have contributed to more accurate modeling of the emission event distributions,

leading to improvements in image reconstruction quality. Additionally, the dual-energy attenuation correction for 511keV and 1,157keV photons has proven effective in enhancing the accuracy of activity distribution quantification, providing more reliable image results. A crucial component of the pipeline is the use of a NN that translates the histo-images, generated from raw PET data, into the final high-resolution reconstructed images. This step significantly improves the quality of the images by refining details and reducing noise, while maintaining structural accuracy. The integration of the NN has proven essential in bridging the gap between the histo-image and the final reconstructed image, ensuring that the proposed approach offers meaningful improvements in quality over traditional TOF-MLEM images. While the improvements are incremental, they highlight the potential of 3- γ -PET systems for more accurate and precise imaging, particularly with isotopes like ^{44}Sc . This work lays a solid foundation for further optimization of 3- γ -PET imaging, with the opportunity to explore real-time clinical applications. However, the issue of positron range, which degrades image quality at smaller resolutions, remains a challenge. Future research will focus on addressing this limitation to improve the performance of 3- γ -PET in small-scale imaging applications.

APPENDIX A EDGE CLASSIFICATION

In [13] the graph is built using two separate matrices that define how messages are passed between nodes. The sender and receiver matrices, respectfully denoted $\mathbf{R}_s \in \mathbb{R}^{N \times N_e}$ and $\mathbf{R}_r \in \mathbb{R}^{N \times N_e}$, are defined as

$$[\mathbf{R}_s]_{n,l} = \begin{cases} 1 & \text{if edge } l \text{ departs from node } n \\ 0 & \text{otherwise} \end{cases}$$

and

$$[\mathbf{R}_r]_{n,l} = \begin{cases} 1 & \text{if edge } l \text{ arrives at node } n \\ 0 & \text{otherwise} \end{cases}$$

For example the sender and receiver matrices corresponding to the graph in Figure 11(a) are

$$\mathbf{R}_s = \begin{matrix} & e_1 & e_2 & e_3 & e_4 & e_5 & e_6 \\ \begin{matrix} o_1 \\ o_2 \\ o_3 \end{matrix} & \begin{bmatrix} 1 & 0 & 1 & 0 & 0 & 0 \\ 0 & 1 & 0 & 0 & 1 & 0 \\ 0 & 0 & 0 & 1 & 0 & 1 \end{bmatrix} \end{matrix}$$

and

$$\mathbf{R}_r = \begin{matrix} & e_1 & e_2 & e_3 & e_4 & e_5 & e_6 \\ \begin{matrix} o_1 \\ o_2 \\ o_3 \end{matrix} & \begin{bmatrix} 0 & 1 & 0 & 1 & 0 & 0 \\ 1 & 0 & 0 & 0 & 0 & 1 \\ 0 & 0 & 1 & 0 & 1 & 0 \end{bmatrix} \end{matrix}$$

which should be read for example (first column of \mathbf{R}_s and \mathbf{R}_r) as “ e_1 sends information from o_1 to o_2 ”.

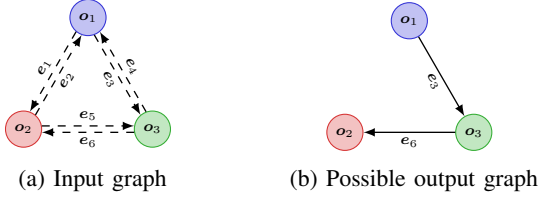


Fig. 11: (a) Fully connected graph used as an input for the GNN; (b) possible output of the GNN.

The first step in the design of an IN is to create a message matrix \mathbf{M} defined as

$$\mathbf{M} = [\mathbf{R}_s^\top \mathbf{O}, \mathbf{R}_r^\top \mathbf{O}] \in \mathbb{R}^{N_e \times 2N_f}.$$

where $[\cdot, \cdot]$ denotes the horizontal concatenation of two matrices with the same number of rows, the total number of directed edges is $N_e = N(N-1)$. Each row in \mathbf{M} corresponds to an edge and contains $2N_f$ features.

In a second step we encode the information carried in each edge into an *effect vector* of dimension N_{eff} via a NN $f_R : \mathbb{R}^{2N_f} \mapsto \mathbb{R}^{N_{\text{eff}}}$ (we used $N_{\text{eff}} = 50$ as suggested in Battaglia *et al.* [13]) which maps each row of \mathbf{M} to an N_{eff} -dimensional row vector (In the original paper Battaglia *et al.* [13] f_R is referred to as a *relation-centric network* as it operates on edges and encodes relations values). By repeating the operation on each row, f_R maps \mathbf{M} to an $N_e \times N_{\text{eff}}$ matrix denoted \mathbf{E} referred to as the *effect matrix*. Each row in \mathbf{E} represents a latent vector of effect for each node on its neighbor.

In a third step the cumulative effect of interactions received by each node is stored in a $N \times N_{\text{eff}}$ matrix $\bar{\mathbf{E}}$ defined as

$$\bar{\mathbf{E}} = \mathbf{R}_r \mathbf{E},$$

and we define the $N \times (N_f + N_{\text{eff}})$ matrix

$$\mathbf{C} = [\mathbf{O}, \bar{\mathbf{E}}].$$

Each row in \mathbf{C} contains the node’s features combined with the interaction effects. An object-centric function f_O maps the $N_f + N_{\text{eff}}$ features for each of the N nodes to a 10-dimensional vector, resulting in a $N \times 10$ matrix which is then flattened into a $10N$ -dimensional column vector. We used an edge model $f_E : \mathbb{R}^{10N} \rightarrow \mathbb{R}^{N_e}$ which maps the new node features vector to a vector of N_e weights, each weight corresponding to an

edge. We used sigmoid activation function in order to give a score between 0 and 1 for each edge.

We thus defined a mapping $\mathbf{F}_\vartheta : \mathbb{R}^{N \times N_f} \rightarrow [0, 1]^{N_e}$ where the parameter ϑ encompasses those of f_R , f_O and f_E .

APPENDIX B

PROPAGATION OF ENERGY AND SPATIAL UNCERTAINTIES ALONG THE LOR

To address the spatial and energy uncertainties that cause blurring along the LOR in 3- γ -PET imaging, we have developed a DREP module to determine σ_{mix}^\pm in Equation (3). This module accounts for both energy and spatial measurement uncertainties in the estimation of the Compton scattering angle and its propagation to the LOR.

A. Propagation of Energy Measurement Uncertainty

Given an initial photon energy E_{init} and a deposited photon energy E_1 at first interaction. The Compton scattering equation in terms of the deposited photon energy is given by 2. To find the uncertainty in the scattering angle θ_C due to the uncertainty in the measured energy, we first take the derivative of $\cos(\theta_C)$ with respect to E_1 :

$$\frac{d(\cos(\theta_C))}{dE_1} = -\frac{m_e c^2}{(E_{\text{init}} - E_1)^2}.$$

The uncertainty in $\cos(\theta_C)$ is then given by:

$$\begin{aligned} \Delta \cos(\theta_{C,\text{energy}}) &= \left| \frac{d(\cos(\theta_C))}{dE_1} \right| \Delta E_1 \\ &= \left| -\frac{m_e c^2}{(E_{\text{init}} - E_1)^2} \right| \Delta E_1. \end{aligned}$$

Finally, we convert this to the uncertainty in θ_C :

$$\begin{aligned} \Delta \theta_{C,\text{energy}} &= \frac{\Delta \cos(\theta_{C,\text{mes}})}{\sin(\theta_C)} \\ &= \frac{\left| -\frac{m_e c^2}{(E_{\text{init}} - E_1)^2} \right| \Delta E_1}{\sin(\theta_C)}. \end{aligned}$$

This equation shows how the error in the measured photon energy propagates to the uncertainty in the scattering angle.

B. Mixing Energy and Spatial Measurement Uncertainties

In a study on the detector resolution using the XEMIS-1 [20] and XEMIS-2 [23] systems, it was shown that the spatial resolution contribution to the scatter angle error is almost constant and is approximately $\Delta \theta_{C,\text{spatial}} = 1.2^\circ$.

Inspired from [8], we consider variations in the angle θ_C due to energy and spatial uncertainties:

$$\theta_{C,\text{energy}}^\pm = \theta_C \pm \Delta \theta_{C,\text{energy}}, \quad \theta_{C,\text{spatial}}^\pm = \theta_C \pm \Delta \theta_{C,\text{spatial}}$$

These variations influence the intersection points of the Compton cone with the LOR, resulting in the coordinates $(x_{\text{energy}}^+, x_{\text{energy}}^-, x_{\text{spatial}}^+, x_{\text{spatial}}^-)$.

We define the blurring on the LOR for each uncertainty as follows:

$$\sigma_{\text{energy}}^\pm = |x - x_{\text{energy}}^\pm|, \quad \sigma_{\text{spatial}}^\pm = |x - x_{\text{spatial}}^\pm|$$

Finally, we combine these uncertainties using the root sum square (RSS) method, for the positive variation,

$$\sigma_{\text{mix}}^+ = \sqrt{(\sigma_{\text{energy}}^+)^2 + (\sigma_{\text{spatial}}^+)^2}, \quad (4)$$

and the negative variation:

$$\sigma_{\text{mix}}^- = \sqrt{(\sigma_{\text{energy}}^-)^2 + (\sigma_{\text{spatial}}^-)^2}. \quad (5)$$

REFERENCES

- [1] J. Kist, B. de Keizer, M. van der Vlies, A. Brouwers, D. Huysmans, F. van der Zant, R. Hermesen, M. Stokkel, O. Hoekstra, and W. Vogel, "Other members of the THYROPET study group are john mh de klerk. 124i PET/CT to predict the outcome of blind 131i treatment in patients with biochemical recurrence of differentiated thyroid cancer; results of a multicenter diagnostic cohort study (thyropet)," *J Nucl Med*, vol. 57, no. 5, pp. 701–7, 2016.
- [2] C. Müller, M. Bunka, J. Reber, C. Fischer, K. Zhernosekov, A. Türler, and R. Schibli, "Promises of cyclotron-produced ^{44}Sc as a diagnostic match for trivalent β -emitters: In vitro and in vivo study of a ^{44}Sc -DOTA-folate conjugate," *Journal of nuclear medicine*, vol. 54, no. 12, pp. 2168–2174, 2013.
- [3] P. Thirolf, C. Lang, and K. Parodi, "Perspectives for highly-sensitive PET-based medical imaging using β γ coincidences," *Acta Physica Polonica A*, vol. 127, no. 5, pp. 1441–1444, 2015.
- [4] L. G. Manzano, S. Bassetto, N. Beaupere, P. Briend, T. Carlier, M. Cherel, J.-P. Cussonneau, J. Donnard, M. Gorski, R. Hamanishi, *et al.*, "XEMIS: A liquid xenon detector for medical imaging," *Nuclear Instruments and Methods in Physics Research Section A: Accelerators, Spectrometers, Detectors and Associated Equipment*, vol. 787, pp. 89–93, 2015.
- [5] L. G. Manzano, J. Abaline, S. Acounis, N. Beaupere, J. Beney, J. Bert, S. Bouvier, P. Briend, J. Butterworth, T. Carlier, *et al.*, "XEMIS2: A liquid xenon detector for small animal medical imaging," *Nuclear Instruments and Methods in Physics Research Section A: Accelerators, Spectrometers, Detectors and Associated Equipment*, vol. 912, pp. 329–332, 2018.
- [6] T. Yamaya, E. Yoshida, H. Tashima, A. Tsuji, K. Nagatsu, M. Yamaguchi, N. Kawachi, Y. Okumura, M. Suga, and K. Parodi, *Whole gamma imaging (WGI) concept: Simulation study of triple-gamma imaging*, 2017.
- [7] D. Giovagnoli, A. Bousse, N. Beaupere, C. Canot, J.-P. Cussonneau, S. Diglio, A. Iborra Carreres, J. Masbou, T. Merlin, E. Morteau, Y. Xing, Y. Zhu, D. Thers, and D. Visvikis, "A pseudo-TOF image reconstruction approach for three-gamma small animal imaging," *IEEE Transactions on Radiation and Plasma Medical Sciences*, vol. 5, no. 6, pp. 826–834, 2021. DOI: 10.1109/TRPMS.2020.3046409.
- [8] E. Yoshida, H. Tashima, K. Nagatsu, A. B. Tsuji, K. Kamada, K. Parodi, and T. Yamaya, "Whole gamma imaging: A new concept of PET combined with compton imaging," *Physics in Medicine & Biology*, vol. 65, no. 12, p. 125013, 2020.
- [9] U. G. Oberlack, E. Aprile, A. Curioni, V. Egorov, and K.-L. Giboni, "Compton scattering sequence reconstruction algorithm for the liquid xenon gamma-ray imaging telescope (Ixe-grit)," in *Hard X-Ray, Gamma-Ray, and Neutron Detector Physics II*, SPIE, vol. 4141, 2000, pp. 168–177.
- [10] G. Pratz and C. S. Levin, "Bayesian reconstruction of photon interaction sequences for high-resolution PET detectors," *Physics in Medicine & Biology*, vol. 54, no. 17, p. 5073, 2009.
- [11] A. Zoglauer and S. E. Boggs, "Application of neural networks to the identification of the compton interaction sequence in compton imagers," in *2007 IEEE Nuclear Science Symposium Conference Record*, vol. 6, 2007, pp. 4436–4441. DOI: 10.1109/NSSMIC.2007.4437096.
- [12] M. Andersson, "Gamma-ray tracking using graph neural networks," Ph.D. dissertation, 2021.
- [13] P. W. Battaglia, R. Pascanu, M. Lai, D. Rezende, and K. Kavukcuoglu, *Interaction networks for learning about objects, relations and physics*, 2016. eprint: arXiv:1612.00222.
- [14] W. Whiteley, V. Panin, C. Zhou, J. Cabello, D. Bharkhada, and J. Gregor, "FastPET: Near real-time reconstruction of PET histo-image data using a neural network," *IEEE Transactions on Radiation and Plasma Medical Sciences*, vol. 5, no. 1, pp. 65–77, 2020.
- [15] P. Isola, J.-Y. Zhu, T. Zhou, and A. A. Efros, "Image-to-image translation with conditional adversarial networks," pp. 1125–1134, 2017.
- [16] M. D. Cirillo, D. Abramian, and A. Eklund, "Vox2vox: 3d-gan for brain tumour segmentation," in *Brainlesion: Glioma, Multiple Sclerosis, Stroke and Traumatic Brain Injuries: 6th International Workshop, BrainLes 2020, Held in Conjunction with MICCAI 2020, Lima, Peru, October 4, 2020, Revised Selected Papers, Part I 6*, Springer, 2021, pp. 274–284.
- [17] S. Jan, G. Santin, D. Strul, *et al.*, "GATE: A simulation toolkit for PET and SPECT," *Physics in Medicine & Biology*, vol. 49, no. 19, p. 4543, 2004.
- [18] E. Aprile and T. Doke, "Liquid xenon detectors for particle physics and astrophysics," *Reviews of Modern Physics*, vol. 82, no. 3, p. 2053, 2010.
- [19] Y. Zhu, M. Abaline, S. Acounis, N. Beaupère, J. Beney, J. Bert, S. Bouvier, P. Briend, J. Butterworth, T. Carlier, *et al.*, "Scintillation signal in xemis2, a liquid xenon compton camera with 3γ imaging technique," in *Proceedings of International Conference on Technology and Instrumentation in Particle Physics 2017: Volume 2*, Springer, 2018, pp. 159–163.
- [20] L. G. Manzano, "Optimization of a single-phase liquid xenon compton camera for 3γ medical imaging," Ph.D. dissertation, Ecole des Mines de Nantes, 2016.
- [21] W. P. Segars, G. Sturgeon, S. Mendonca, *et al.*, "4D XCAT phantom for multimodality imaging research," *Medical physics*, vol. 37, no. 9, pp. 4902–4915, 2010.
- [22] D. Ulyanov, A. Vedaldi, and V. Lempitsky, "Deep image prior," in *Proceedings of the IEEE conference on computer vision and pattern recognition*, 2018, pp. 9446–9454.
- [23] D. Giovagnoli, "Image reconstruction for three-gamma PET imaging," Ph.D. dissertation, Ecole nationale supérieure Mines-Télécom Atlantique, 2020.